

Height Measurement Accuracy of ERS-1 SAR Interferometry

Antonio Moccia

Facoltà di Ingegneria, Università degli Studi di Napoli "Federico II"

Salvatore Esposito

CO.RI.S.T.A.

P.le Tecchio 80, 80125 Naples, Italy

Marco D'Errico

Facoltà di Ingegneria, Università degli Studi di Napoli "Federico II"

ABSTRACT

Several authors have proven that the ERS-1 images obtained along nearly parallel orbits are adequate for interferometric applications. Consequently, ERS-1 allows to evaluate and test the height measurement accuracy achievable by repeat-track interferometry. Since the authors' main interest is in Global Topographic Mapping, this paper shows the method adopted to derive a Digital Elevation Model of an extended area, by using an ERS-1 interferometric pair. In particular, the procedures for geometric registration, baseline estimation and phase unwrapping are described in details. Then a theoretical analysis, which derives the height error budget for point targets, is proposed. Our results show that baseline uncertainty and phase noise give the major error contribution to the computed height, which does not satisfy the international map accuracy standards.

INTRODUCTION

SAR Interferometry is considered one of the most promising techniques to satisfy various scientific applications which require a Digital Elevation Model (DEM) over large areas of the world (Topographic Science Working Group, 1988). Since the first airborne successful experiments (Graham, 1974; Zebker and Goldstein, 1986), several authors have proposed and/or tested spaceborne SAR interferometric systems (Hirosawa and Kobayashi, 1986; Gabriel and Goldstein, 1988; Gabriel et al. 1989; Prati et al., 1990; Moccia and Vetrella, 1992; Sander and Vetrella, 1993).

Among these techniques repeat-track interferometry has a significant advantage: it uses a single antenna which observes the same area from two orbits, separated in the cross-track direction. This allows to surpass some of the problems connected to the simultaneous use of two spaceborne antennas, i.e., mainly cost and complexity. Neverthe-

less, several aspects of repeat-track interferometry need further investigations, such as: baseline indetermination and variation, decorrelation due to the changes in backscatter characteristics of the terrain, non-simultaneous interferometric images, orbit selection for adequate coverage, achievable height accuracy.

ERS-1 is an existing satellite which allows low cost SAR Interferometry using parallel orbits, with a 3-day or 35-day repeat cycle, slightly shifted in cross-track and vertical directions due to orbital perturbations. Specifically, Single-Look Complex (SLC) images processed by using the Verification Mode Processor (VMP) at ESA/ESRIN (Frascati) have proven to be adequate for interferometric fringes generation (ERS-1 Fringe Working Group, 1992).

The intent of this paper is to investigate the potentiality of repeat-track interferometry for Global Topographic Mapping, i.e. generation of a high resolution Digital Elevation Model (DEM) of the Earth surface which satisfies international map accuracy standards (Welch and Marko, 1981). To this end the height accuracy of a DEM obtained by processing an ERS-1 SLC interferometric pair is evaluated. The various steps of the interferometric processing necessary to generate a DEM are described in details. Finally, a theoretical model of the height error budget for point targets is proposed, both to derive the system performance of a repeat-track SAR interferometer and to gain further insight into the accuracy of our ERS-1 DEM.

1. INTERFEROMETRIC PAIR REGISTRATION

The area selected for the DEM generation is a subset of Naples ERS-1 test site consisting of 1024 slant range pixels and 4096 single-look azimuth pixels. Fig. 1 shows this area after a coherent four-azimuth-look procedure. An image vertical reflection has been applied because the image was taken during the descending phase of the ERS-1 orbit with

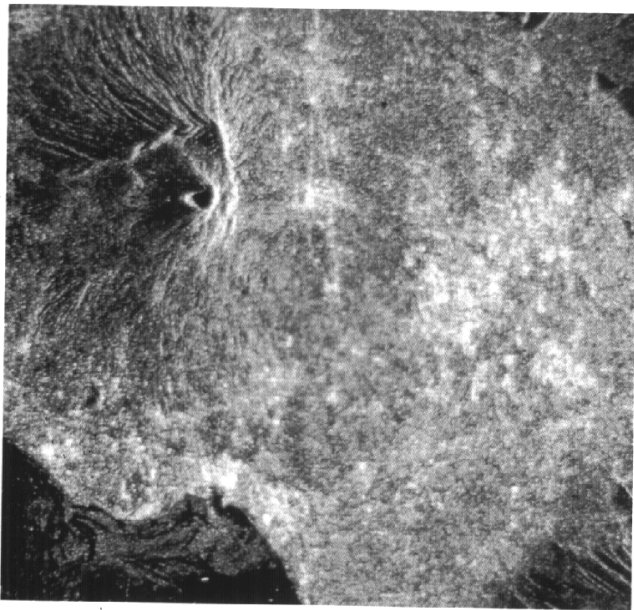


Fig. 1 - Selected area (Naples test site).

a clockwise off-nadir angle with respect to the satellite velocity vector. This means that the near range is on the right side of the image, which is correctly west-east oriented.

This area represents an interesting test site for decorrelation studies because it includes bare soils (Vesuvius volcano), agriculture and urban areas, and the shoreline, which is an useful reference for interferometry. In addition, scattered elevation points of this area digitised by the Istituto Geografico Militare Italiano (IGMI), the official Italian geographical institute, are available and can be used to validate the generated DEM.

The first step of the processing is an approximate registration based on a visual inspection of the two images candidate to form an interferogram. This is accomplished by a simple two-dimensional (2-D) rigid translation, derived by means of a limited number of Ground Control Points (GCPs) identified in the SLC images. This preliminary registration is performed only for images taken with an adequate interferometric baseline, roughly computed by using the ERS-1 propagated state vectors listed in the SAR product annotations report by ESA ESRIN. Moreover, it allows to speed up the successive sub-pixel registration, which is more sophisticated and time-consuming.

At this stage the interferogram, formed by multiplying one registered image by the complex conjugate of the other, exhibits large decorrelated areas and is not adequate for DEM generation, because of significant misregistration problems (Li and Goldstein, 1990). However it allows to check the previously computed baseline and, consequently, to confirm the usefulness of the interferometric pair by

estimating the baseline component normal to the slant range direction (Prati and Rocca, 1990). Of course this procedure can be successfully applied only if it is possible to evaluate the fringe-slant-range spacing over a sufficiently large, correlated, and approximately flat area.

On the basis of this analysis, we selected the 27-AUG-1991 and 5-SEP-1991 passes, during the orbits 592 and 721.

The procedure for sub-pixel registration of our test area is based on the automatic identification of a large number of GCPs. This task cannot be easily accomplished with SAR data covering large areas (Dowman, 1992) and requires a careful strategy. The first step consists in the division of the two VMP SLC images in subareas. Then, the coordinates of the maximum amplitude point are identified in each subarea. The images in proximity of each pair of homologous bright points are oversampled in order to evaluate the sub-pixel shift between the two images. This shift is different in range and azimuth directions over the whole image, as expected.

Among the various proposed oversampling techniques (Shafer and Rabiner, 1973), we focused our attention on fast Fourier transforms (FFTs) and cubic splines. FFTs are computationally efficient and allow accurate oversampling of 2-D sequences with respect to an interpolation formula given for band-limited signals, as shown by Sathyanarayana *et al.* (1990) who evaluated the mean square error with respect to the original sampled signal. Nevertheless, several problems still exist. For instance, it is necessary to have a large number of GCPs in order to improve the sub-pixel geometric registration, which, consequently, implies the application of 2-D FFTs for oversampling many small adjacent regions. This approach cannot be easily accomplished because a significant error is introduced in the zero-filling procedure when the Doppler centroid frequency of a short sequence is evaluated. On the other hand, wherever a larger area is considered, besides the computer memory and time requirements, the variation of the Doppler centroid frequency from near to far range must be taken into account.

As shown by Hou and Andrews (1978), cubic B-splines allow more accurate and efficient 2-D interpolations with respect to classical polynomial methods. In fact, they minimise the least square error of the function values and of its first and second derivatives. We found that, when compared to the FFT procedure, the cubic B-spline technique is not much more computationally intensive and is easily adaptable to small areas. In addition, it is accurate and advantageous also in the successive image resampling because it allows to compute the function value after taking into account the pixel coordinates transformed in floating point format, without the nearest neighbour approximation and without the need of two large images simultaneously on line. To compare FFTs and cubic B-splines we performed a set of tests using as input an area of limited dimension (256×256 single-look complex pixels), relative to bare soils exhibiting

a satisfactory coherence coefficient (Monti Guarnieri *et al.*, 1992), also when only the previous visual registration is carried out. This allowed us both to overcome problems connected to Doppler frequency variation and to suppose that the differences in the resulting coherence coefficient were basically due to the adopted co-registration procedure. First of all we performed an eight-times two dimensional oversampling of both images by cubic B-splines and FFTs. Then we evaluated the sub-pixel shifts necessary to accomplish the geometric registration by means of the computationally intensive technique proposed by Gabriel and Goldstein (1988), that we will analyse more thoroughly later on. In the first case the image resampling was carried out by computing the function value by means of cubic B-spline interpolation, whereas in the latter case the nearest neighbour technique was applied. Finally, we computed the coherence coefficient before and after the coherent multi-look, as shown in tab. 1. Our results show that the two techniques are basically equivalent, but in the case of cubic B-splines it is possible to make significantly more efficient the procedure from the computational point of view. To this end we can:

- 1. compute the sub-pixel shift by oversampling only core memory resident sub-areas of the two images;
- 2. perform the geometric registration by resampling only small sub-areas of the first image;
- 3. obtain straight the interferogram and, then, oversample it before applying the multi-look procedure.

Table 1 - Coherence coefficients for the two analysed oversampling techniques.

| | no multi-look | coherent multi-look |
|----------------|---------------|---------------------|
| cubic B-spline | 40.7 % | 60.3 % |
| FFT | 39.8 % | 57.4 % |

At the end of this procedure we obtained a coherence coefficient equal to 56.4%, which is a quite satisfactory value. Of course, in the proposed sequence, the low-pass filtering connected to a band-limited resampling is applied only to the first of the two images forming the interferogram. This could accomplish a coherence reduction, due to the high frequencies still present in the second, unchanged image. To gain further insight into this aspect, we applied our procedure using a different second image, obtained by cubic B-spline resampling the previous one after a 0.5 pixel shift in both directions. In this case we obtained a coherence coefficient reduction of only 0.7%. Consequently, we applied the above procedure, using two-dimensional cubic B-splines both to oversample for GCP identification and to resample the image during the geometric registration.

The next step of this procedure is the evaluation of the sub-pixel shifts between the two oversampled images, that we perform by using the following techniques:

- 1. cross-correlation of the pixel amplitudes;
- 2. maximum value of the coherence coefficient (Monti Guarnieri *et al.*, 1992), i.e. cross-correlation of the pixel complex values (Li and Goldstein, 1990);
- 3. evaluation of the maximum amplitude or of the maximum signal-to-noise ratio (SNR) in the fringe spectrum (Gabriel and Goldstein, 1988);
- 4. minimisation of the average fluctuation of the phase difference image (Lin *et al.*, 1992).

We found that the first technique is quite simple and effective, because it provides GCPs over most of the image. The second technique gives satisfactory results only for strong point targets, while it may fail otherwise. The third and fourth techniques are more effective for extended targets and when the fringe pattern is well defined, which is not our case over most of the interferogram. In conclusion, we can say that the four techniques give basically the same result when the correlation is satisfactory, whereas the first technique, which is not phase dependent, is more reliable in the case of poor correlation. Considering that the accuracy of the geometric transformation increases significantly when a large number of GCPs distributed over the whole image is available, we applied the first technique obtaining thereby 172 GCPs.

Tab. 2 lists the column (range bin) and row (azimuth) shifts measured in ten-times-oversampled pixels. As expected, the sub-pixel shifts are small because they are computed after the preliminary coarse registration. In particular, the residual shift is of the order of the original SLC image pixel. It is worth noting that the azimuth shift is practically constant, whereas the shift in range direction decreases of about half a SLC pixel, from near range to far range of this subset of the ERS-1 frame. In fact the two orbits are not exactly parallel and the ERS-1 attitude is not exactly the same. Moreover, the two images were focused separately, each one with its Doppler centroid frequency and bandwidth variations from near to far range. The ground range direction is, therefore, geometrically different in the two images. The shaded areas shown in tab. 2 are representative of significantly decorrelated regions, whereby it is not possible to compute any shift by using the four proposed methods. For example, this is the case of the sea surface, as it can be inferred by comparing fig. 1 and tab. 2.

The geometric registration of the interferometric pair is then performed by means of bicubic polynomials, whose coefficients are computed with least square approximation, using as input the 172 sub-pixel shifts listed in tab. 2 (Kratky, 1972; Konecny, 1976). The root mean square error is less than 1/10 of the ten-times-resampled pixel both in range and in azimuth direction.

Table 2 - Sub-pixel range and azimuth shifts between the ten-times-oversampled images.

| | | RANGE BIN | | | | | | | | | | | |
|---|------|-----------|-------|-------|-------|-------|-------|-------|-------|-------|-------|-------|------|
| | | 1 | 100 | 200 | 300 | 400 | 500 | 600 | 700 | 800 | 900 | 1000 | 1024 |
| A Z I M U T H P O S I T I O N | 1 | 10,10 | 9,11 | 10,10 | 11,10 | 12,10 | 12,10 | 13,11 | 13,10 | | | | |
| | 200 | 10,10 | 10,10 | 10,10 | 11,10 | | 12,11 | 12,10 | 14,10 | | | | |
| | 400 | 10,10 | 10,10 | 10,10 | 12,9 | 12,10 | 12,10 | 13,10 | 13,10 | | 15,10 | | |
| | 600 | | 11,10 | 10,9 | 10,9 | 12,10 | 12,10 | 13,10 | | 15,10 | 15,10 | 15,10 | |
| | 800 | | | | 12,9 | 12,10 | 12,10 | 13,10 | 14,10 | 14,11 | 15,9 | 14,9 | |
| | 1000 | 10,10 | | | 12,9 | | | 12,10 | 13,10 | 14,10 | 14,10 | 15,10 | |
| | 1200 | 10,10 | 9,10 | 12,9 | | 12,10 | 13,10 | 12,10 | 14,10 | 14,10 | 14,10 | 15,9 | |
| | 1400 | 9,10 | | | | | 13,10 | 13,10 | 13,10 | 14,10 | 15,10 | | |
| | 1600 | | 9,10 | | 12,9 | | 13,10 | 13,10 | 13,10 | 15,10 | 14,10 | 15,10 | |
| | 1800 | 10,10 | 9,10 | | | | 12,10 | 13,10 | 13,10 | 14,10 | 15,9 | 15,9 | |
| | 2000 | | 10,10 | 9,10 | | 11,11 | 12,10 | 12,10 | 14,10 | 13,10 | 15,10 | 15,10 | |
| | 2200 | 10,10 | 9,10 | 9,10 | 11,11 | 12,10 | 12,10 | 12,10 | 14,10 | 15,9 | 14,10 | 15,10 | |
| | 2400 | 10,11 | 10,10 | 10,10 | 11,10 | 11,10 | 12,10 | 12,10 | 13,11 | 14,10 | 14,10 | 15,10 | |
| | 2600 | 9,9 | 10,10 | 10,10 | 11,10 | 12,10 | 12,10 | 13,10 | 14,10 | | 15,10 | 14,9 | |
| | 2800 | | 11,11 | 10,10 | 11,10 | 11,10 | 12,10 | | 13,10 | 14,10 | 15,10 | 15,10 | |
| | 3000 | | 11,11 | 11,10 | 11,10 | 11,11 | 12,10 | 12,10 | 14,10 | 14,10 | 15,9 | 16,10 | |
| N | 3200 | | | 11,10 | 11,10 | 11,11 | 11,10 | 12,10 | 13,10 | 14,10 | 14,11 | 15,10 | |
| | 3400 | | | 10,11 | 11,10 | 12,10 | 12,10 | 13,11 | 13,10 | 13,10 | 15,10 | 16,10 | |
| | 3600 | | | | | 12,10 | 12,10 | 13,10 | 13,9 | 13,9 | 15,10 | | |
| | 3800 | | | | | 12,9 | 13,10 | 13,10 | 13,10 | | | | |
| | 4000 | | | | | | 12,9 | 13,10 | 13,10 | 14,10 | | | |

The resulting interferogram is oversampled four times by using the same technique and, finally, a coherent multilook (16 azimuth-looks, 4 range-looks) is executed averaging the complex values in order to give the maximum likelihood estimation of the phase (Rodriguez, 1992; Werner *et al.*, 1992). The decorrelated regions listed in tab. 2 are clearly visible in fig. 2, which shows the resulting interferogram.

2. ERS-1 BASELINE ESTIMATION

The estimation of the ERS-1 baseline is a fundamental step to derive height measurements. Different techniques have been proposed: based on the use of an array of precisely located corner reflectors (Monti Guarnieri *et al.*, 1992), on the knowledge of ERS-1 orbit data (De Fazio *et al.*, 1992), on the integration of topographic tie points with ERS-1 state vectors (Werner *et al.*, 1992).

Our procedure uses the ERS-1 Restituted Orbit Data (100 state vectors per orbit computed at 1 minute interval) and the ERS-1 Propagated State Vectors (5 state vectors per SLC VMP image computed at 1.750 second interval) to derive the ERS-1 state vector components as a function of time (t):

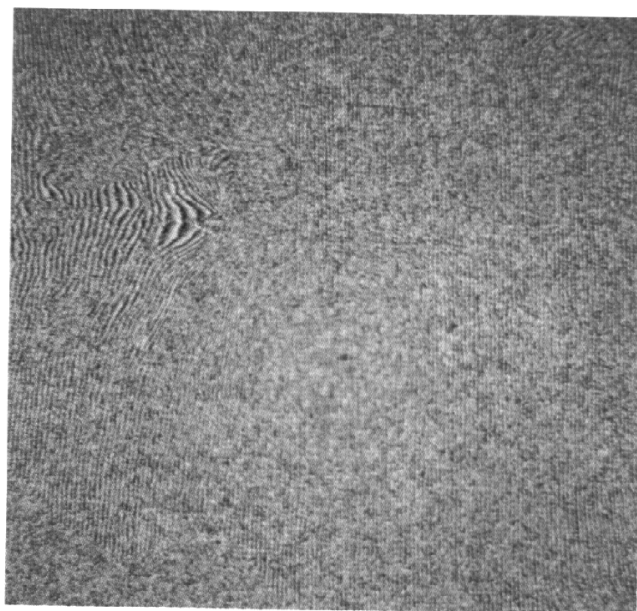


Fig. 2 - Resulting interferogram.

$$[X_i(t) \ Y_i(t) \ Z_i(t) \ \dot{X}_i(t) \ \dot{Y}_i(t) \ \dot{Z}_i(t)] \quad (1)$$

for $i=1,2$, i.e. for the two orbits of the interferometric pair. As shown in fig. 3, X,Y,Z is a geocentric, right-handed, Earth-fixed, and hence rotating, reference frame, in which the Z axis is directed northwards and the XZ plane coincides with the zero longitude meridian (Greenwich). Consequently, in this reference frame, the ERS-1 orbit is a three-dimensional curve.

A least square approximation is adopted to obtain the coefficients of a sixth order polynomial for each component of the state vector, using 9 input points. With reference to fig. 3, the 9 points are P_{ij} ($i=1,2$ $j=1,5$), and R_{ik} ($i=1,2$ $k=1,4$). P_{ij} represents the j -th ERS-1 position along the i -th orbit, during the acquisition of the images forming the interferogram and given by the Propagated State Vectors, which are listed in the SAR Product Annotations Report:

$$[X_{ij} \ Y_{ij} \ Z_{ij} \ \dot{X}_{ij} \ \dot{Y}_{ij} \ \dot{Z}_{ij}] \quad (2)$$

and R_{ik} represents the k -th ERS-1 position along the i -th orbit, given by the two values of the Restituted Orbit State Vector, computed immediately before and after the acquisition of the two images.

The geographical coordinates of a ground control point T , precisely identified in the co-registered images, are, then,

derived by a conventional topographic map. The latitude, longitude and height of T allow to compute its geocentric coordinates (X_T, Y_T, Z_T) (Moccia and Vetrella, 1986). The Doppler frequency of T , when the satellite is in P_{ij} and R_{ik} , is analytically computed as follows:

$$f_{Dil} = - \frac{2}{\lambda} \frac{[\dot{X}_{il}(X_{il} - X_T) + \dot{Y}_{il}(Y_{il} - Y_T) + \dot{Z}_{il}(Z_{il} - Z_T)]}{[(X_{il} - X_T)^2 + (Y_{il} - Y_T)^2 + (Z_{il} - Z_T)^2]^{1/2}} \quad (3)$$

where λ is the wavelength, and $l=1,9$. Again, a least square approximation (sixth order polynomial using 9 input points) yields the GCP Doppler frequency as a function of time $f_{Di}(t)$ $i=1,2$. A sixth order polynomial makes negligible the root mean square error of the interpolated input points, both for the state vector components and for the Doppler frequencies, and gives a three-dimensional curve which is very close to a theoretical orbit.

The clutterlock algorithm allows to compute the GCP Doppler frequency in the two SLC VMP images (Li et al., 1985). The value derived considering the azimuth power spectrum of the line containing the GCP is affected by errors due to:

1. Doppler Centroid frequency ambiguity;
2. numerical problems;
3. noise.

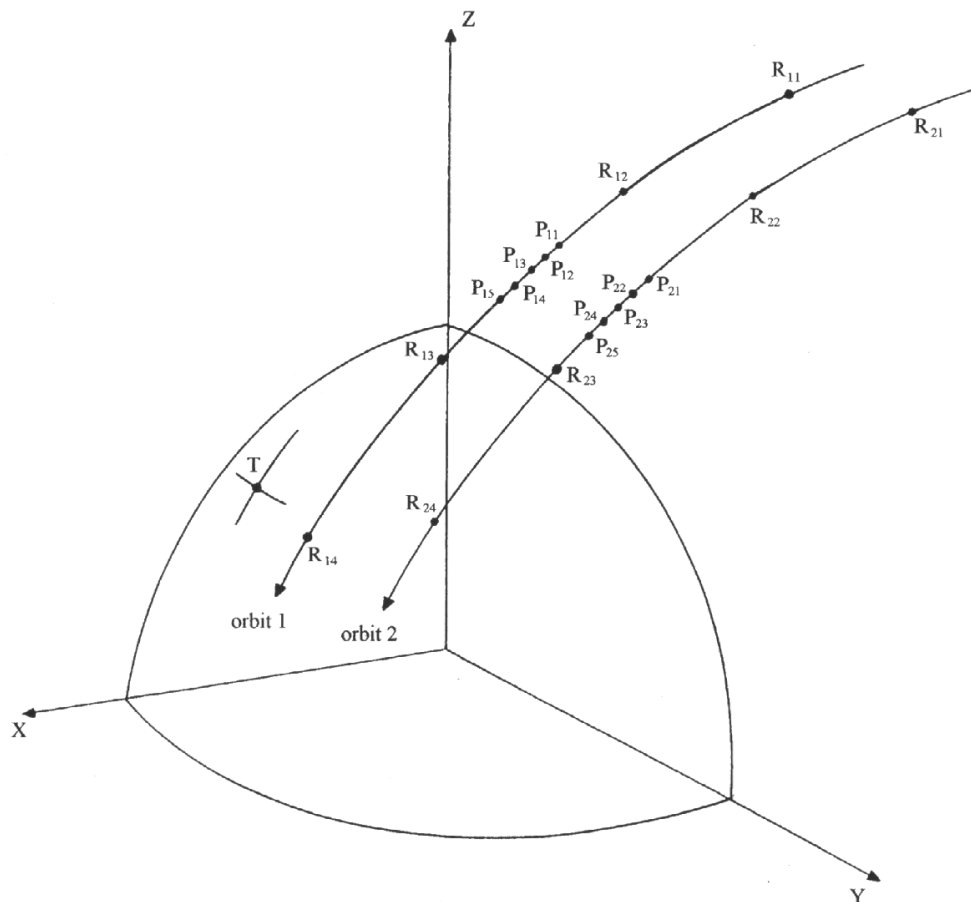


Fig. 3 - Geometry for ERS-1 baseline estimation.

The first error source, described by Raney (1986), is neglected, because the programmed yaw steering makes the SAR antenna approximately orthogonal to the ERS-1 ground track (Attema, 1991).

Items 2 and 3 are necessarily related. The clutterlock procedure, adopted to determine the centre of the azimuth power spectra, may fail due to the presence of bright targets or to a low or variable signal-to-noise ratio. As an example, figs 4 and 5 show the Doppler frequency computed from near range to far range of the two input images. The frequencies have been obtained by applying the clutterlock algorithm to a full synthetic aperture centred on the GCP position. The estimation can be improved by averaging several azimuth power spectra (Li *et al.*, 1985), or by approximating the frequencies from near range to far range with proper functions. Applying this second technique, we obtain two lines by least square approximation of the Doppler frequencies, computed by the clutterlock algorithm. fig. 6 puts in evidence the diversity of the approximated Doppler frequency and rate between the two considered passes. As expected (Raney, 1986), due to orbit and attitude differences, the spacecraft-target relative velocity vector and the target position vector with respect to the spacecraft are not equal in the two images. Although upper order polynomials reduce the root mean square error computed for the input frequency values, the straight line provides the most regular and reliable cross-track variation from the geometrical point of view. These lines allow to derive the GCP Doppler centroid frequency.

By interpolating the Doppler frequencies along the orbit ($f_{D_i}(t)$), we compute the time along the orbit which corresponds to the GCP Doppler centroid frequency. Then, the relative ERS-1 state vector is derived by using the sixth order polynomials. Finally, the state vector allows the computation of the three baseline components (vertical B_z , along-track B_x , cross-track B_y) with respect to an ERS-1 fixed reference frame along the orbit 1, by means of a transformation matrix. As shown in fig. 7, this right-handed reference frame has the z-axis coincident with the spacecraft-Earth centre direction and the y-axis perpendicular to the plane defined by the spacecraft velocity and position vectors.

Tab. 3 shows the parameters adopted to estimate the baseline components, using as input a GCP close to the Vesuvius crater (GCP#1).

More GCPs could improve the baseline estimate, in particular if they are distributed over the whole image, both in range and in azimuth direction. It is necessary, however, to account for baseline variation within the interferometric pair. Due to orbit and attitude differences, each GCP is focused in a different position of the two SLC VMP images, depending on its geographical coordinates. Tab. 4 reports the baseline components estimated by using three different GCPs,

Table 3 - Parameters adopted for baseline estimation using as input GCP#1.

| | |
|---------------|----------------|
| latitude | 40° 19' 9.56" |
| longitude | 14° 24' 55.02" |
| height (m) | 754 |
| X_T (Km) | 4682.31462 |
| Y_T (Km) | 1203.54543 |
| Z_T (Km) | 4147.82258 |
| f_{D1} (Hz) | 411.22 |
| f_{D2} (Hz) | 423.41 |
| B_x (m) | -51.444 |
| B_y (m) | -171.218 |
| B_z (m) | 103.206 |

approximately at the same range but at different azimuth position (fig. 8). B_x and B_y component variations are due to ERS-1 yaw steering, which accounts for the Earth tangential velocity function of the latitude. Since B_z component is due only to orbit decay and eccentricity, it is practically constant in the interferometric pair.

3. TWO-DIMENSIONAL PHASE UNWRAPPING

With reference to fig. 7, the baseline estimation procedure computes also the ERS-1 semi-major axis (a) and the slant range (R_{IGCP}) between the antenna and the GCP. For the sake of clarity, it is worth noting that in fig. 7 the positive

Table 4 - Baseline estimation using three different GCPs.

| | B_x (m) | B_y (m) | B_z (m) |
|--------|-----------|-----------|-----------|
| GCP #2 | -55.488 | -171.184 | 103.209 |
| GCP #1 | -51.444 | -171.218 | 103.206 |
| GCP #3 | -45.855 | -171.433 | 103.209 |

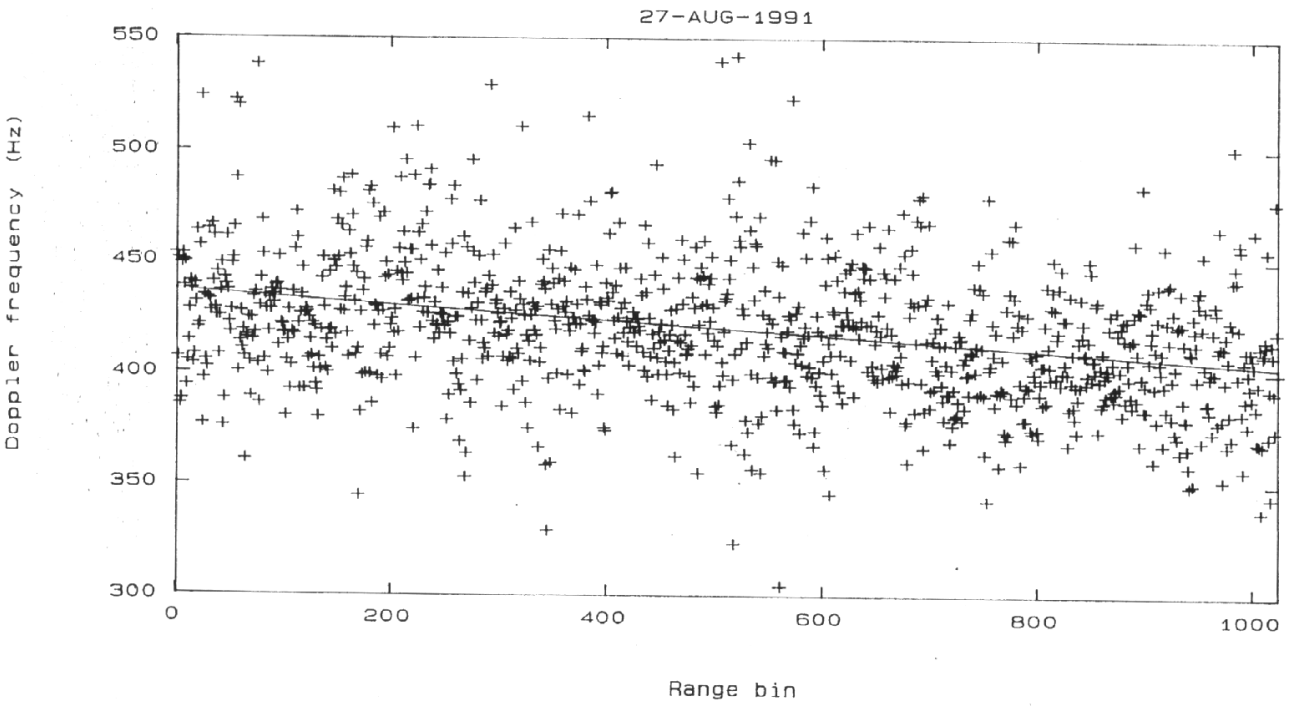


Fig. 4 - Doppler frequency from near range to far range, image acquisition time: 27-AUG-1991.

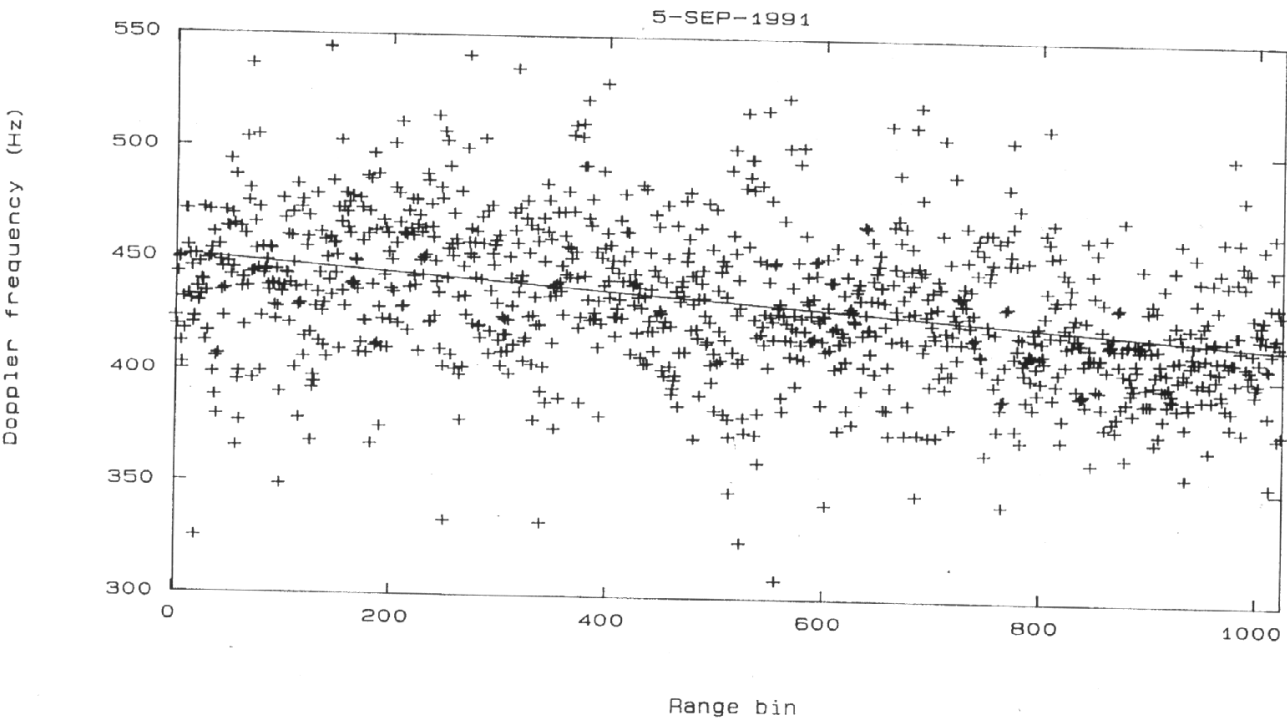


Fig. 5 - Doppler frequency from near range to far range, image acquisition time: 5-SEP-1991.

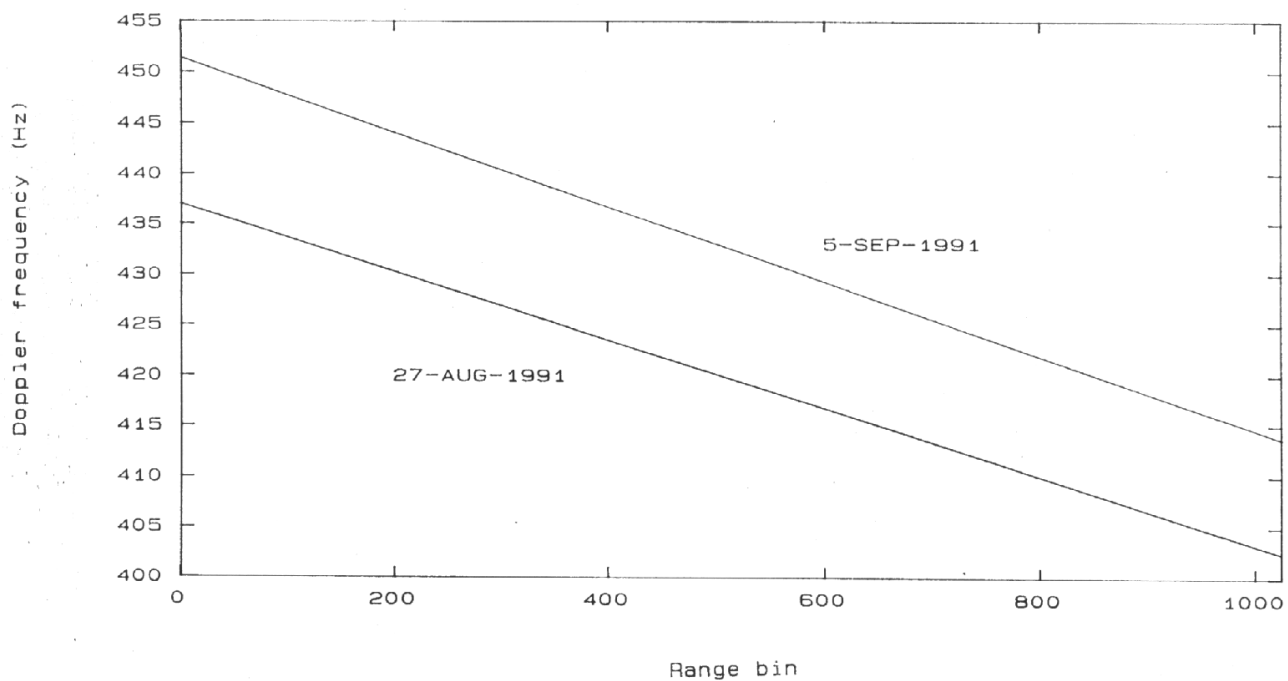


Fig. 6 - Lines obtained by least square approximation of the Doppler frequencies.

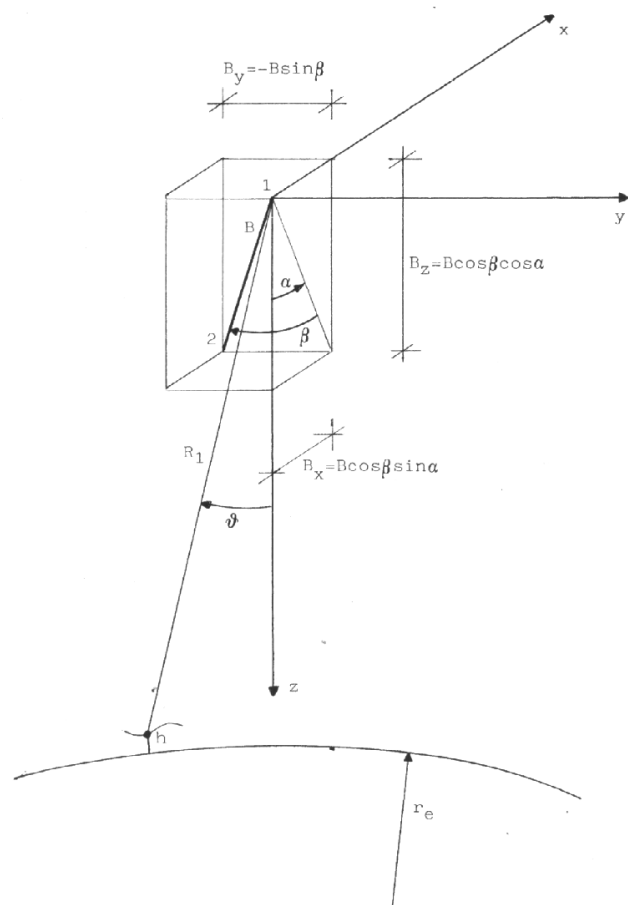


Fig. 7 - ERS-1-fixed reference frame and baseline components.

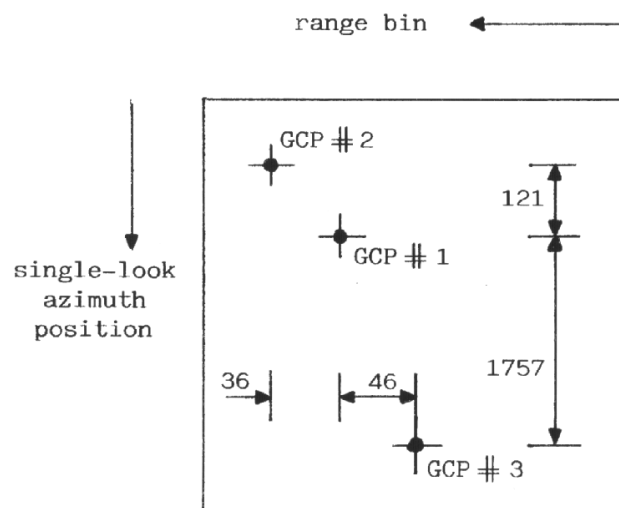


Fig. 8 - Location of the three GCP in the interferometric pair.

baseline in-plane (α) and out-of-plane (β) angles and the positive antenna side-looking angle (ϑ) are plotted, whereas ERS-1 has a negative (counterclockwise) side-looking angle. The side-looking angle corresponding to the GCP location (ϑ_{GCP}) is computed as follows:

$$\vartheta_{GCP} = \cos^{-1} \left[\frac{a^2 + R_{1GCP}^2 - (r_e + h_{GCP})^2}{2aR_{1GCP}} \right] \quad (4)$$

where r_e is the Earth local radius and h_{GCP} is the GCP height. Since the phase difference Φ between two homologous points is given by:

$$\begin{aligned} \Phi &= \frac{2\pi}{\lambda} 2(R_1 - R_2) = \\ &= \frac{4\pi}{\lambda} \left\{ R_1 - \left[(-B_x)^2 + (-R_1 \sin \vartheta - B_y)^2 + (R_1 \cos \vartheta - B_z)^2 \right]^{1/2} \right\} \equiv \\ &\equiv \frac{4\pi}{\lambda} \left[(B_z \cos \vartheta - B_y \sin \vartheta) - \frac{B^2}{2R_1} \right] \end{aligned} \quad (5)$$

it is possible to solve the 2π ambiguity on the GCP, and, then, to start the 2D phase unwrapping.

Two procedures have been implemented:

1. identification of local errors (residues) and connection of the residues with cuts to avoid error propagation (Goldstein et al., 1988);
2. fringe line detection by means of edge enhancement techniques (Lin et al., 1992).

In both cases various decorrelated areas avoid a satisfactory solution of the phase ambiguity problem. As an example, the green areas in fig. 9 represent the isolated regions after the cuts necessary to prevent error propagation. In addition, a large number of positive and negative residues (cyan) are still present in the correlated region (blue). Fig. 10 shows the result of an edge enhancement procedure, which compares the phase mean value to the phase of each pixel inside a window moving on the blue area of fig. 9. Many broken fringe lines are visible in fig. 10, and, since they are too close together, it is difficult to implement any automatic connecting technique.

Fig. 11 shows an interferogram in which the phase pattern of a spherical Earth at constant terrain height has been removed. In this case the fringe pattern is due primarily to the height differences with respect to the GCP. Since the phases are displayed except for 2π integer multiples, this result is not affected by error propagations during phase unwrapping, at least from a qualitative point of view, but it does not allow to derive quantitative height measurements over the whole image.

In the following we focus our attention on a small region, close to the Vesuvius crater and including GCP#1, to derive

a digital elevation model. In this area, which is a subset of tion. The height (h) of each pixel, above a local spherical Earth, is computed as follows:

$$h = \left[(a - R_1 \cos \vartheta)^2 + (R_1 \sin \vartheta)^2 \right]^{1/2} - r_e \quad (6)$$

where the side-looking angle is given by the analysis of the interferometric image (eq. (5), and the slant range (R_1) is

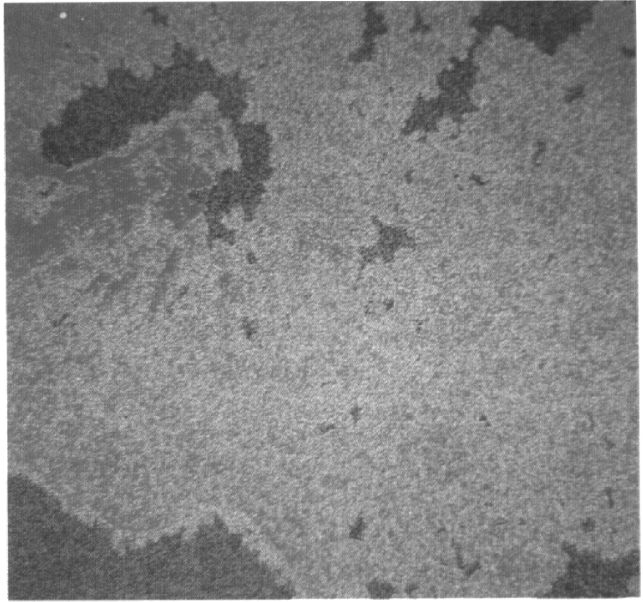


Fig. 9 - Determination of residues (cyan) and isolated areas (green) during the 2D phase unwrapping procedure.

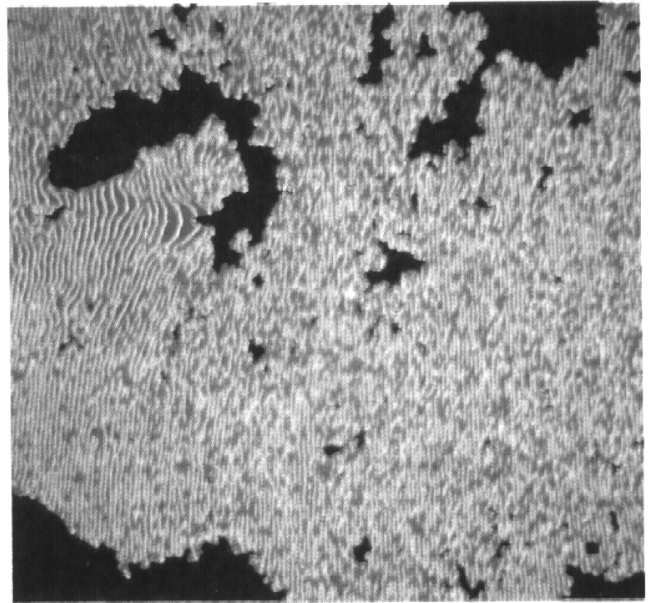


Fig. 10 - Fringe edge enhancement to improve the phase unwrapping.

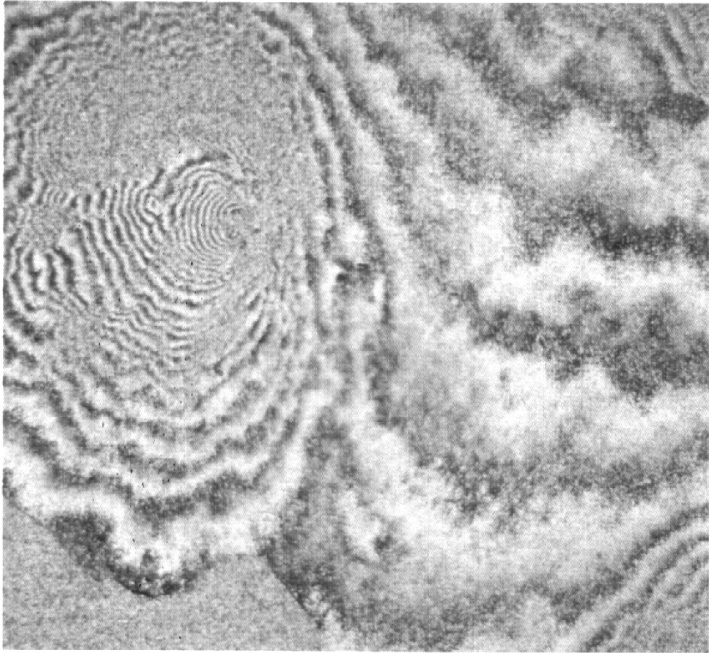


Fig. 11 - Interferogram after the subtraction of the GCP#1 phase.

evaluated with respect to R_{IGCP} . Fig. 12 shows the attained DEM. In order to validate the DEM height accuracy, we use the digitised scattered elevation points given by the Italian Istituto Geografico Militare (IGMI). The IGMI performs the

automatic acquisition of the orographic high quality transparencies (scale 1:25,000), by means of a linear array at a resolution of 100 microns. Consequently, we have a sequence of isolated height points and a sequence of corners, that are the end points of straight lines representing the contour lines, with an approximation of 1/10 mm at map scale. The height root mean square error (rmse) is $\pm 3m$. A computer program allows us to obtain the terrain elevation and slope in a digital raster format, using the digitised points as input (Vetrella and Moccia, 1989). This procedure gives a DEM with a height rmse of $\pm 3m$ with respect to the input height points. Then, a polynomial transformation function between the ERS-1 image row and column indices and the DEM UTM (Universe Transverse Mercator) coordinates is found by using GCPs. The co-registration is obtained with a rmse of ± 2 ERS-1 pixels. By comparing 175 height values between the two DEMs of the selected test area, we attain a rmse of 34m (fig. 13). A more accurate estimate of the height differences can be obtained considering only the 14 available IGMI input points (tab. 5). In this case the rmse is 23m. This result must be carefully assessed. Several error sources affect the computed height, and it is useful to exploit their relative importance. To this end the next paragraph presents an error budget derived under the assumption of point targets.

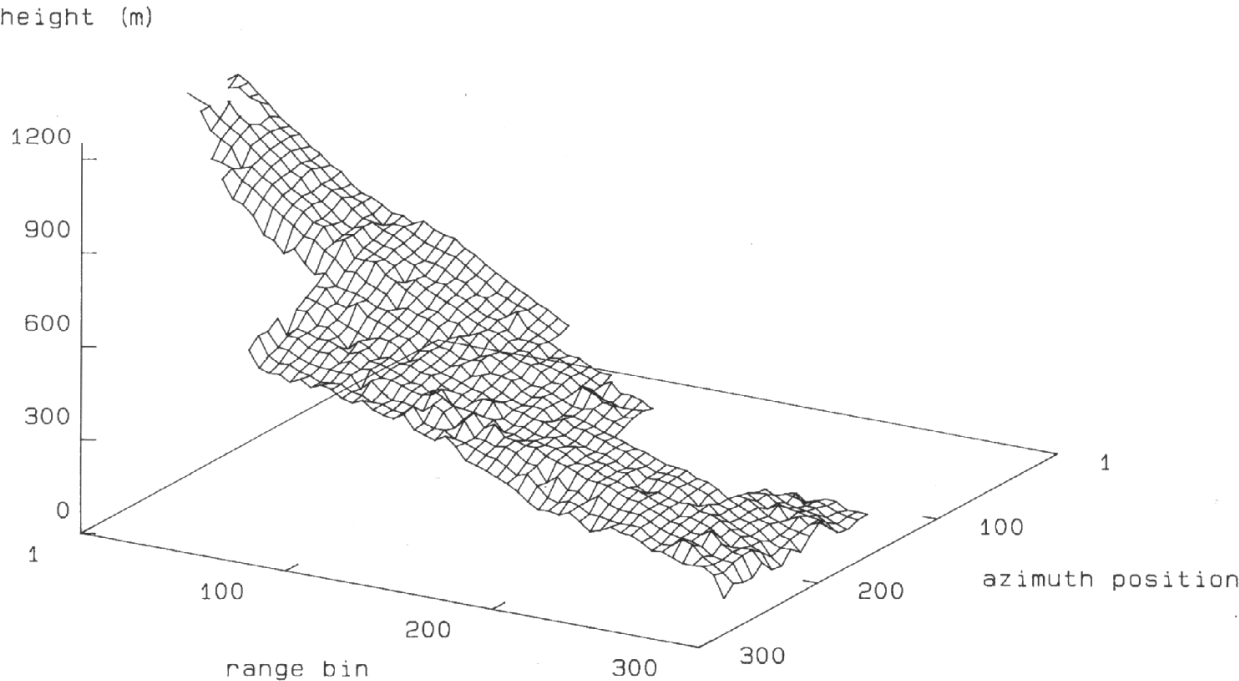


Fig. 12 - Digital Elevation Model of an area close to the Vesuvius crater.

Table 5 - ERS-1 derived heights and IGMI input points.

| Point Number | SAR DEM | | | IGM DEM | | |
|-----------------|---------|---------|------------|-------------|--------------|------------|
| | Range | Azimuth | Height (m) | UTM Est (m) | UTM Nord (m) | Height (m) |
| 1 | 21 | 8 | 1157 | 451376 | 4519548 | 1150 |
| 2 | 26 | 9 | 1132 | 451260 | 4519562 | 1075 |
| 3 | 22 | 11 | 1147 | 451363 | 4519509 | 1150 |
| 4 | 24 | 11 | 1112 | 451311 | 4519510 | 1125 |
| 5 | 27 | 14 | 1110 | 451246 | 4519484 | 1075 |
| 6 | 26 | 16 | 1137 | 451272 | 4519445 | 1100 |
| 7 | 25 | 17 | 1112 | 451298 | 4519419 | 1125 |
| 8 | 25 | 19 | 1142 | 451310 | 4519380 | 1150 |
| 9 | 26 | 19 | 1119 | 451284 | 4519393 | 1125 |
| 10 | 26 | 21 | 1139 | 451284 | 4519354 | 1125 |
| 11 | 25 | 22 | 1144 | 451310 | 4519328 | 1150 |
| 12 | 27 | 23 | 1128 | 451271 | 4519328 | 1125 |
| 13 | 22 | 26 | 1152 | 451400 | 4519249 | 1175 |
| 14 | 25 | 27 | 1138 | 451322 | 4519250 | 1150 |

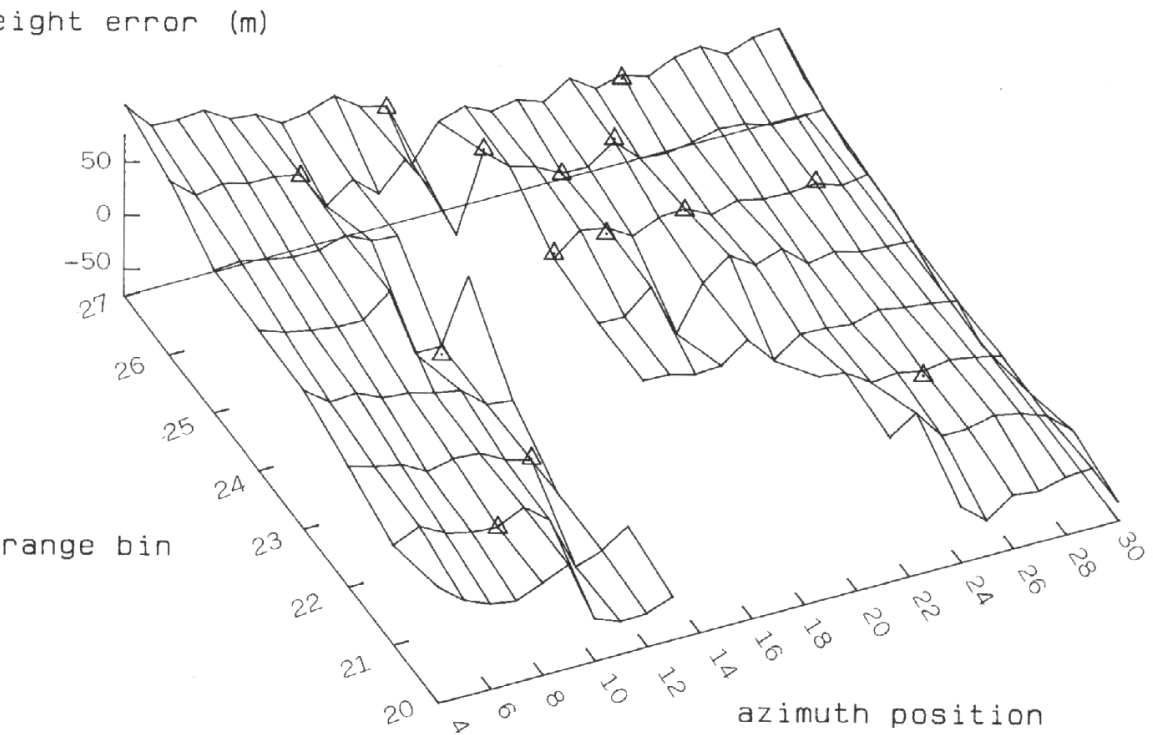


Fig. 13 - DEM height errors; the triangles are relative to the IGMI input points.

4. REPEAT-TRACK INTERFEROMETRY ERROR BUDGET

In order to gain further insight into repeat-track interferometry, in the following we derive its theoretical height measurement accuracy.

The point target assumption allows to obtain results which are useful for evaluating the system impulse response and are appropriate to analyse the performance of the radar when viewing man-made targets (calibration). For a single point target on a dark background (e.g. a corner reflector), we need only consider the single reflected phasor received at the antennas from the target. Multilook processing is not helpful in this case, since the return is coherent over all the looks. The extended-surface case, which is more appropriate for natural terrain height mapping, has been analysed by Li and Goldstein (1990), Rodriguez and Martin (1992), and Zebker and Villasenor (1992).

We assume that systematic errors have been essentially removed by some small set of GCPs, so we consider only random errors caused by noise and geometric uncertainties. The height measurement uncertainty (σ_h) under the assumption of uncorrelated parameters is given by (Li and Goldstein, 1990):

$$\sigma_h^2 = \left(\frac{\partial h}{\partial a} \right)^2 \sigma_a^2 + \left(\frac{\partial h}{\partial R_1} \right)^2 \sigma_{R_1}^2 + \left(\frac{\partial h}{\partial \vartheta} \right)^2 \sigma_{\vartheta}^2 + \left(\frac{\partial h}{\partial B_x} \right)^2 \sigma_{B_x}^2 + \left(\frac{\partial h}{\partial B_y} \right)^2 \sigma_{B_y}^2 + \left(\frac{\partial h}{\partial B_z} \right)^2 \sigma_{B_z}^2 \quad (7)$$

where σ_a , σ_{R_1} , σ_{ϑ} , σ_{B_x} , σ_{B_y} , and σ_{B_z} are the uncertainties in the measurement of the semi-major axis, the slant range, the side-looking angle, and the baseline components,

$$\frac{\partial h}{\partial a} = \frac{a - R_1 \cos \vartheta}{q} \quad O(10^\circ) \quad (8a)$$

$$\frac{\partial h}{\partial R_1} = \frac{R_1 - a \cos \vartheta}{q} \quad O(10^\circ) \quad (8b)$$

$$\frac{\partial h}{\partial \vartheta} = \frac{a R_1 \sin \vartheta}{q} \quad O(10^5 m) \quad (8c)$$

$$\frac{\partial h}{\partial B_x} = \frac{a B_x \sin \vartheta}{qp} \quad O(10^{-1}) \quad (8d)$$

$$\frac{\partial h}{\partial B_y} = \frac{(B_y + R_1 \sin \vartheta) a \sin \vartheta}{qp} \quad O(10^3) \quad (8e)$$

$$\frac{\partial h}{\partial B_z} = \frac{(B_z - R_1 \cos \vartheta) a \sin \vartheta}{qp} \quad O(10^3) \quad (8f)$$

and

$$\begin{cases} q = (a^2 + R_1^2 - 2aR_1 \cos \vartheta)^{1/2} \\ p = B_z \sin \vartheta + B_y \cos \vartheta \end{cases} \quad (9)$$

The orders of magnitude $O(x)$ listed in eqs. (8) have been computed by using the values of the first ERS-1 passage over GCP#1 (tab. 6). The uncertainties in ϑ , B_y , B_z are clearly of major importance. It is worth noting that only the slant range error can be immediately neglected (eqs. (7),(8b)). In fact, s_{R1} is of the order of 30cm, because it depends on the clock timing error and the atmospheric delay. In addition, since the orbit semi-major axis and the baseline components are derived contemporaneously, by means of the above described procedure, we can assume the same order of magnitude for the uncertainties in a , B_x , B_y , B_z .

Table 6 - ERS-1 parameters adopted to derive the height error budget.

| | | |
|-------------------------|------------------------|------------|
| semi-major axis (Km) | | 7152.32511 |
| Earth local radius (Km) | | 6369.25672 |
| near range | slant range (Km) | 833.24382 |
| | side looking angle (°) | 18.954 |
| far range | slant range (Km) | 841.33064 |
| | side looking angle (°) | 20.312 |
| GCP#1 | slant range (Km) | 839.25162 |
| | side looking angle (°) | 19.978 |

σ_{ϑ} stems from two sources: phase error in the pixel and location error within the pixel.

The quantization of the side-looking angle due to the chirp sampling frequency provides the second contribution to the angular uncertainty. This effect is negligible for point and extended targets. In the first case, it is possible to reduce the location uncertainty by oversampling the return signal. In the case of extended targets we have the averaging effect over the natural surface.

With reference to the first contribution, by assuming large Signal-to-Noise Ratio (SNR) and Rician statistics on the received phasors, the standard deviation of the phase difference is (Goodman, 1975):

$$\sigma_{\Phi} = \frac{1}{\sqrt{SNR}} \quad (10)$$

and, consequently, the angular uncertainty is given by:

$$\sigma_{\theta} = \frac{1}{2\pi p \sqrt{SNR}} \quad (11)$$

Assuming $SNR=19.5$ dB, which is a value adequate for point targets, σ_{θ} is of the order of 10^{-5} rad and, consequently, the relative height uncertainty is of the order of few meters (eqs. (7),(8c)).

In conclusion, the major contribution comes from B_y and B_z components (eqs. (7),(8e),(8f)). This result and the DEM rmse, computed in the previous paragraph, demonstrate that the accurate baseline estimation is a key point which requires further investigations for an operational use of repeat-track interferometry.

In addition, the height error due to σ_{B_y} and σ_{B_z} is range dependent (eqs. 8e, 8f) and increases of about 20% (10%) for a B_y (B_z) constant uncertainty from near to far range of the analysed interferometric pair (1024 range bins).

A further aspect to be taken into account is the geometric registration between the interferogram, or the ERS-1-based DEM, and the DEM adopted to check the height accuracy. Although this post-processing aspect does not affect the height error budget, the resultant rmse strongly depends on the misregistration between the two DEMs, and on the height accuracy of the "reference" DEM. As an example, in the previous paragraph we showed that the height rmse computed by using only the height points (23m) is better than the value derived by comparing the two DEMs (34m). Of course, in the first case the rmse is calculated with reference to a smaller set of control points. In both cases the root mean square errors are also affected by misregistration problems. This is particularly true for our test site due to the morphological complexity of Vesuvius area, which presents significant slopes. It is worth noting that Coulson et al. (1992) make this error negligible by using 19 corner reflectors, precisely located by GPS, and by averaging several height values computed for each point target using different interferometric pairs.

CONCLUSIONS

This paper presented an interferometric application of ERS-1 SLC images, that we conducted within the ERS-1 Fringe Working Group activities. Our main objective was to study the potentiality of repeat-track interferometry for the generation of a DEM of the whole Earth surface, which satisfies topographic mapping standards.

After the selection of an interferometric pair of Naples test site, the geometrical co-registration, the baseline components estimation, and the phase unwrapping, we computed the height rmse of the ERS-1 DEM with respect to digitised

scattered elevation points. We observed that several decorrelated areas did not permit the generation of a well defined interferogram. Moreover, the accuracy of the DEM, obtained on a subset of the input image, was not satisfactory, mainly due to baseline uncertainty and phase noise.

Nevertheless, the ERS-1 experience represents an interesting and useful test-bed which can be used to put in evidence several peculiarities of repeat-track interferometry, such as the baseline and time decorrelation effects. In particular, the orbit design is a key point which requires a difficult trade-off study involving the repetitivity and mission lifetime adequate for global coverage, and the variation of resolution, baseline and height accuracy as a function of the orbital position and latitude. Obviously, in the ERS-1 case it is not possible to select and/or change the baseline, but it is worth noting that SAR interferometry is basically a very effective ERS-1 by-product.

In addition several aspects of our interferometric processing need further investigations, such as:

1. Use of different test areas and/or ERS-1 passes.
2. Use of more GCPs (distributed over the whole image), of the shoreline, and of more sophisticated ancillary data and orbital models (for example including attitude data) to reduce the baseline uncertainty.
3. Improvement of the phase unwrapping procedure, in particular of the techniques to reconstruct the fringe edges and to reduce the height error along these lines. This could be accomplished, for example, by using the path determination technique proposed by Prati et al. (1990), which has been demonstrated to be very effective when there are a lot of residues (Sowter and De Groof, 1992), or by using the coherence coefficients to cancel decorrelated areas.
4. Improvement of the procedure to co-register the ERS-1 DEM and the conventional topographic data, after their conversion to raster format. For example, we plan to use a simulation program which accounts for orbital dynamics and sensor viewing geometry, and computes the geographical coordinates of the intersection of each line-of-sight with the Earth surface (Moccia et al., 1991).
5. More extensive validation and comparison of the procedure adopted for interferometric pair registration.

In conclusion, we think that the operational use of repeat-track interferometry for Global Topographic Mapping is unlikely. On the other hand, provided that an adequate baseline is available, ERS-1 and ERS-2 interferometric data could be used for obtaining low resolution DEMs, useful where no topographic data exists.

ACKNOWLEDGEMENTS

The authors are sincerely grateful to Drs. S. Coulson, M. Doherty and L. Marelli (ESA/ESRIN) for providing ERS-1

VMP data, within the ERS-1 Fringe Working Group activities.

The use of the digitised elevation points was authorised by the Istituto Geografico Militare Italiano (no. 3759 29/1/1993).

REFERENCES

- Attema E.P.W., 1991. "The Active Microwave Instrument On-Board the ERS-1 Satellite", *Proc. of the IEEE*, vol. 79, no. 6, pp. 791-799.
- Coulson S., Doherty M., Hartl P., Reich M., Prati C. and Rocca F., 1992. "Validation of SAR Interferometry for small motions estimation", presented at the CEOS Workshop on SAR Calibration, 21-25 Sept., Ottawa, Canada, pp. 8.
- De Fazio M., Esposito S. and Vinelli F., 1992. "Experimental Activities on ERS-1 Reference Data Set", *Proc. of 1st Workshop ERS-1 Fringe Working Group*, ESA ESRIN, Frascati, pp. 20.
- Dowman I., 1992. "The geometry of SAR images for geocoding and stereo applications", *Int. J. Remote Sensing*, vol. 13, no. 9, pp. 1609-1617.
- ERS-1 Fringe Working Group, 1992. *Proceed. of 1st Workshop*, ESA ESRIN, Frascati, Italy, ESRIN/ERS Missions Section.
- Gabriel A.K. and Goldstein R.M., 1988. "Crossed orbit interferometry: Theory and experimental results from SIR-B", *Int. J. Remote Sensing*, vol. 9, no. 8, pp. 857-872.
- Gabriel A.K., Goldstein R.M. and Zebker H.A., 1989 "Mapping small elevation changes over large areas: differential radar interferometry", *J. Geophys. Res.*, vol. 94, no. B7, pp. 9183-9191.
- Goldstein R.M., Zebker H.A. and Werner C.L., 1988. "Satellite radar interferometry: Two-dimensional phase unwrapping", *Radio Science*, vol. 23, no. 4, pp. 713-720.
- Goodman J.W., 1975. "Statistical properties of laser speckle patterns", in Dainty J.C., Ed., *Laser Speckle and Related Phenomena*, New-York: Springer-Verlag.
- Graham L.C., 1974. "Synthetic interferometric radar for topographic mapping", *Proc. IEEE*, vol. 62, pp. 763-768.
- Hirosawa H. and Kobayashi N., 1986. "Terrain height measurement by synthetic aperture radar with an interferometer", *Int. J. Remote Sensing*, vol. 7, no. 3, pp. 339-348.
- Hou H.S. and Andrews H.C., 1978. "Cubic spline for image interpolation and digital filtering", *IEEE Trans. on acoustics, speech, and signal processing*, vol. 26, no. 6, pp. 508-517.
- Konecny G., 1976. "Mathematical Models and Procedures for the Geometric Restitution of Remote Sensing Imagery", invited paper, XIII Congress of the Int. Soc. for Photogrammetry, Helsinki, pp. 33.
- Kratky V., 1972. "Image Transformations", *Photogrammetric Engineering*, vol. XXXVIII, no. 5, pp. 463-471.
- Li F. and Goldstein R.M., 1990. "Studies of Multibaseline Spaceborne Interferometric Synthetic Aperture Radars", *IEEE Trans. on Geoscience and Remote Sensing*, Vol. 28, no. 1, pp. 88-97.
- Li F., Held D.N., Curlander J.C. and Wu C., 1985. "Doppler Parameter Estimation for Spaceborne Synthetic-Aperture Radars", *IEEE Trans. on Geoscience and Remote Sensing*, vol. 23, no. 1, pp. 47-56.
- Lin Q., Vesecky J.F. and Zebker H.A., 1992. "New Approaches in Interferometric SAR Data Processing", *IEEE Trans. on Geoscience and Remote Sensing*, vol. 30, no. 3, pp. 560-567.
- Moccia A., Vetrella S. and Ponte S., 1991. "Passive and Active Calibrators Characterization by using a Spaceborne SAR System Simulator", *Proc. of the SAR Calibration Workshop*, DLR, Oberpfaffenhofen, Oct. 9th-11th, pp. 26; accepted for publication on *IEEE Trans. on Geoscience and Remote Sensing*, 1993
- Moccia A. and Vetrella S., 1986. "An integrated approach to geometric precision processing of spaceborne high-resolution sensors", *Int. J. Remote Sensing*, vol. 7, no. 3, pp. 349-359.
- Moccia A. and Vetrella S., 1992. "A Tethered Interferometric Synthetic Aperture Radar (SAR) for a Topographic Mission", *IEEE Trans. on Geoscience and Remote Sensing*, vol. 30, no. 1, pp. 103-109.
- Monti Guarnieri A., Parizzi F., Pasquali P., Prati C. and Rocca F., 1992. "Developments in ERS-1 SAR Interferometry", *Proc. of 1st Workshop ERS-1 Fringe Working Group*, ESA ESRIN, Frascati, pp. 16.
- Prati C. and Rocca F., 1990. "Limits to the resolution of elevation maps from stereo SAR images", *Int. J. Remote Sensing*, vol. 11, no. 12, 2215-2235.
- Prati C., Rocca F., Monti Guarnieri A. and Damonti E., 1990. "Seismic Migration For SAR Focusing: Interferometrical Applications", *IEEE Trans. on Geoscience and Remote Sensing*, vol. 28, no. 4, pp. 627-640.
- Raney R.K., 1986. "Doppler properties of radars in circular orbits", *Int. J. Remote Sensing*, vol. 7, no. 9, pp. 1153-1162.
- Rodriguez E.R., 1992. "Maximum likelihood estimation of the interferometric phase from distributed targets", in press, *IEEE Trans. on Geoscience and Remote Sensing*.
- Rodriguez E.R. and Martin J.M., 1992. "Theory and design of interferometric synthetic aperture radars", *IEE PROCEEDING-S-F*, vol. 139, no. 2, pp. 147-159.
- Sander M.J. and Vetrella S., 1993. "Global Topography Mission (GTM) Overview", presented at the EARSeL/CO.R.I.S.T.A. Int. Workshop on SAR Interferometry, Naples, Italy, 18-20 May.
- Sathyanarayana P., Reddy P.S. and Swamy M.N.S., 1990. "Interpolation of 2-D Signals", *IEEE Trans. on Circuits and Systems*, vol. 37, no. 5, pp. 623-625.
- Schafer R.W. and Rabiner L.R., 1973. "A digital signal processing approach to interpolation", *Proc. of the IEEE*, vol. 61, no. 6, pp. 692-702.
- Sowter A. and De Groof H., 1992. "Co-registration and Phase Unwrapping Techniques", *Proc. of 1st Workshop ERS-1 Fringe Working Group*, ESA ESRIN, Frascati, pp. 16.
- Topographic Science Working Group, 1988. "Report to the Land Processes Branch, Earth Science and Application Division, Lunar and Planetary Institute, NASA", Houston, TX, 64 pp.
- Welch R. and Marko W., 1981. "Cartographic potential of a

spacecraft line-array camera system: Stereosat", *Photogrammetric Eng. Remote Sensing*, vol. 47, no. 8, pp. 1173-1185.

Vetrella S. and Moccia A., 1988. "A Procedure for Modeling the Terrain Relief by Using Digitised Topographic Maps", *Geocarto International*, Vol. 3, no. 3, pp. 3-11.

Werner C.L., Goldstein R.M., Rosen P. and Zebker H.A., 1992. "Techniques and Applications of SAR Interferometry for ERS-1: Topographic Mapping, Slope Measurement and Change Detec-

tion", *Proc. of 1st Workshop ERS-1 Fringe Working Group*, ESA ESRIN, Frascati, pp. 11.

Zebker H.A. and Goldstein R.M., 1986. "Topographic mapping from interferometric synthetic aperture radar observations", *J. Geophys. Res.*, vol. 91, no. B5, pp. 4993-4999.

Zebker H.A. and Villasenor J., 1992. "Decorrelation in Interferometric Radar Echos", *IEEE Trans. on Geoscience and Remote Sensing*, vol. 30, no. 5, pp. 950-959.